Equatorial distributions of the plasma sheet ions, their electric and magnetic drifts, and magnetic fields under different interplanetary magnetic field B_z conditions

Chih-Ping Wang,[1] Larry R. Lyons,[1] James M. Weygand,[2] Tsugunobu Nagai,[3] and Richard W. McEntire[4]

Received 22 November 2005; revised 12 January 2006; accepted 19 January 2006; published 21 April 2006.

[1] To understand the nightside plasma sheet structure under different interplanetary magnetic field (IMF) B_z conditions, we have investigated statistically the equatorial distributions of ions and magnetic fields from Geotail when the IMF has been continuously northward or southward for shorter or longer than 1 hour. A dawn-dusk density (temperature) asymmetry with higher density (temperature) on the dawn (dusk) side is seen in the near-Earth plasma sheet during northward IMF, resulting in roughly dawn-dusk symmetric pressure. As southward IMF proceeds, the density asymmetry weakens while the temperature asymmetry maintains, resulting in higher pressure on the dusk side. The plasma sheet is relatively colder and denser near the flanks than around midnight. The flux distributions show that the density asymmetry is due to ions $<\sim$3 keV, and the temperature asymmetry is due to ions above thermal energy. The perpendicular flow shows that ions divert around the Earth mainly through the dusk side in the inner plasma sheet because of westward diamagnetic drift. The magnetic fields indicate that field lines are more stretched during southward IMF. Ions' electric and magnetic drift paths evaluated from the observations show that for thermal energy ions, magnetic drift is as important as electric drift. Comparison of the distributions of the observed phase space density with the evaluated drift paths at different energies indicates that the electric and magnetic drift transport is responsible for the observed dawn-dusk asymmetries in the plasma sheet structure.

Citation: Wang, C.-P., L. R. Lyons, J. M. Weygand, T. Nagai, and R. W. McEntire (2006), Equatorial distributions of the plasma sheet ions, their electric and magnetic drifts, and magnetic fields under different interplanetary magnetic field B_z conditions, *J. Geophys. Res.*, *111*, A04215, doi:10.1029/2005JA011545.

1. Introduction

[2] The transport and energization of the plasma from different source locations results in the spatial structure of the plasma and fields in the plasma sheet and inner magnetosphere. This structure and its variation in location and time in response to changes in the solar wind and interplanetary magnetic field (IMF) are crucial to the formation and dynamic changes of storms, substorms and other disturbances. Additionally, field-aligned currents arise from the spatial gradient of the structure and couple the magnetosphere with the ionosphere, which in turn affects plasma transport and fields. Fundamental aspects of understanding and predicting the structure are determining how to directly relate quantitatively the transport, energization, and source distribution to solar wind and IMF conditions.

[3] It has been theorized that the major entry sites for solar wind plasma into the plasma sheet are located at the distant tail and the flank magnetopause, that the major large-scale transport for the plasma after entering the plasma sheet consists of energy-independent electric drift and energy-dependent magnetic drift, and that the adiabatic energy change associated with the drifts is the major energization process. The electric drift is due to the convection electric field resulting from the coupling of the Earth's magnetosphere with the solar wind and IMF, while the magnetic drift is controlled by the magnetic field configuration, which varies strongly with the IMF and solar wind conditions.

[4] Observations have established overall understanding of the equatorial distributions of the plasma sheet under general conditions [e.g., *Paterson et al.*, 1998; *Kaufmann et al.*, 2004a, 2004b; *Guild et al.*, 2004] and during quiet times [e.g., *Angelopoulos et al.*, 1993; *Angelopoulos*, 1996] on the basis of in situ measurement of ions up to $\sim$40 keV q^{-1}. *Tsyganenko and Mukai* [2003] derived a 2-D dawn-dusk symmetric analytical tail plasma sheet using Geotail data to

[1]Department of Atmospheric and Oceanic Sciences, University of California, Los Angeles, California, USA.
[2]Institute of Geophysics and Planetary Physics, University of California, Los Angeles, California, USA.
[3]Department of Earth and Planetary Sciences, Tokyo Institute of Technology, Tokyo, Japan.
[4]Johns Hopkins University Applied Physics Laboratory, Laurel, Maryland, USA.

0148-0227/06/2005JA011545$09.00

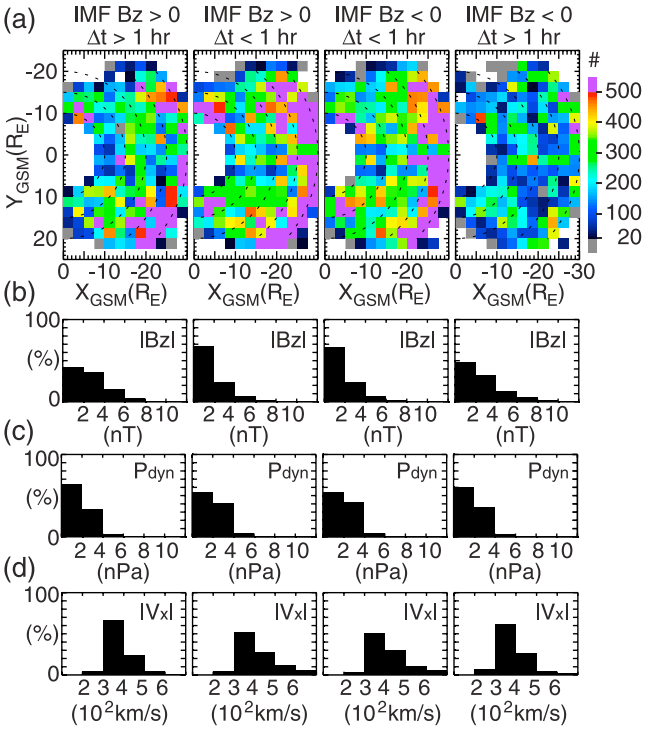

Figure 1. (a) Number of 1 min data measurements, (b) occurrence rate of the IMF $|B_z|$, (c) solar wind dynamic pressure P_{dyn}, and (d) solar wind $|V_x|$ during the four IMF B_z conditions.

show the correlation of the plasma sheet with the solar wind. *Wing and Newell* [1998, 2002] deduced 2-D equatorial plasma sheet distributions for different geomagnetic activities or IMF B_z directions by mapping the low-altitude observations to the equatorial plane using the dawn-dusk symmetric magnetic field from the Tsyganenko 89 model. Observational data have also been analyzed to investigate our physical understanding of the transport and energization in the plasma sheet [e.g., *Garner et al.*, 2003; *Kaufmann et al.*, 2004a], including adiabatic electric and magnetic drifts and other processes, such as fast flows and substorms. Qualitative agreement has been found between the observed structure and the results of simulations that model the electric and magnetic drift of plasma from the tail and flanks [e.g., *Spence and Kivelson*, 1993; *Wang et al.*, 2004].

[5] Among the interplanetary parameters, the IMF B_z has been shown to play a crucial role in solar wind–magnetosphere coupling. The cross–polar cap potential drop is larger with stronger southward IMF but does not change significantly during northward IMF [*Weimer*, 1995]. Ion entry from the flanks appears to be more efficient during northward IMF than southward IMF [e.g., *Fujimoto et al.*, 1998]. Substorm onset is proceeded by a growth phase with IMF being continuously southward for longer than ~30 min. Stronger ring current and geomagnetic disturbances have been observed when a prolonged northward IMF is followed by a sudden southward IMF or magnetosphere compression [*Thomsen et al.*, 2003]. The status of the magnetosphere is found to be correlated with the history of the IMF B_z [e.g., *Terasawa et al.*, 1997]. Therefore to reveal realistically the plasma sheet structure in response to an IMF B_z of different directions and duration allows for quantitative validation of simulations of plasma transport and energization and evaluation of the physical processes that result in the observed plasma sheet.

[6] In this study we investigate statistically the 2-D distribution of the nightside plasma sheet in the equatorial plane when the magnetosphere has been coupled with southward or northward IMF for less than or more than 1 hour. We include ions from ~ 0.021 to 3000 keV measured by Geotail to obtain more accurate plasma pressures and temperatures than did previous studies. We investigate the plasma moments density, temperature, pressure, and perpendicular flow, as well as flux versus particle energy and the magnetic field. We infer the plasma sheet electric field and electric potential from the observed plasma and magnetic field data and evaluate the electric and magnetic drift of different energy ions. We also investigate ion drift paths to understand how the interplay of particle sources in the tail and along the flanks, and the transport of these source particles under different IMF B_z conditions, result in different plasma distributions and to show, by comparing with the distributions of observed phase space density of different energy, that electric and magnetic drift can approximately account for observed dawn-dusk asymmetries in the plasma sheet distributions, and to indicate possible importance of processes other than electric and magnetic drift during southward IMF.

2. Instrumentation and Data

[7] In this study we use Geotail data in GSM coordinates from 1 November 1994 to 30 April 1998 and in the area $|Y| \leq 22.5\ R_E$ and $0 \geq X \geq -30\ R_E$ (the smallest radial distance covered by Geotail is ~8 R_E). Plasma data from two instruments aboard Geotail are used: the ion data from the Low Energy Particle (LEP) instrument [*Mukai et al.*, 1994] that covers the energy range from 21 eV q^{-1} to 46 keV q^{-1} and the proton data from the Energetic Particles and Ion Composition (EPIC) instrument [*Williams et al.*, 1994] that cover the energy range from 46 keV to 3005 keV. Magnetic field data is from the magnetic field (MGF) experiment [*Kokubun et al.*, 1994]. 1 min averages of the plasma and magnetic field data are used.

[8] The IMF and solar wind data from November to December 1994 are from IMP 8 and the data for the rest of the study period are from Wind. The arrival time of the IMF at the subsolar bow shock at (X = 17, Y = 0, Z = 0 R_E) is determined with IMF by calculating the minimum variance direction from the minimum variance analysis technique [*Weimer et al.*, 2003].

[9] Central plasma sheet crossings are defined by plasma pressure (P_{ion}) being larger than magnetic pressure ($P_{mag} = B^2/(2\mu_0)$). We use $V_x > -100$ km s^{-1} to exclude magnetosheath crossings and $|V_\perp| \leq 200$ km s^{-1} to exclude large bursty bulk flow. The data for the central plasma sheet are then sorted into four IMF B_z conditions: the IMF B_z has been continuously (1) northward for more than 1 hour, (2) northward for less than 1 hour, (3) southward for less than 1 hour, and (4) southward for more than 1 hour. The choice of 1 hour is to have roughly similar number of data points for each IMF condition. Finally the IMF-sorted data are averaged over an area of 2.5 R_E × 2.5 R_E in the *X*-*Y* plane. Figure 1 shows the number of 1-min data measure-

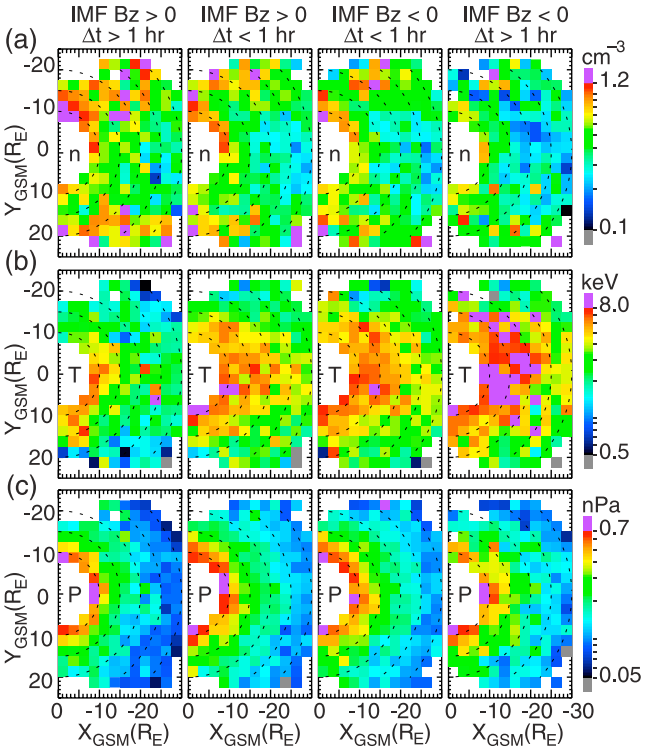

Figure 2. Equatorial distributions of (a) number density, (b) temperature, and (c) plasma pressure during the four IMF B_z conditions.

ments and the occurrence rate of the magnitude of some interplanetary parameters for the four IMF B_z conditions. The relatively fewer number of data points at smaller r is due to Geotail moving faster, thus spending shorter time in the plasma sheet, when closer to its perigee. It can be seen from the occurrence rate that during almost 90% of the period of interest the interplanetary parameters have $|B_z| < 4$ nT, $P_{\rm dyn} < 4$ nPa, and $|V_x|$ between 300 and 500 km s^{-1}.

3. Results and Analysis

3.1. Ion Number Density, Temperature, and Pressure

[10] Figure 2 shows the number density, temperature, and plasma pressure for the four IMF B_z conditions. The overall density can be seen to be higher (lower) during northward (southward) IMF and to increase (decrease) as the northward (southward) IMF proceeds, while the dependence of the overall temperature and pressure on the IMF B_z is opposite to that of density. During northward IMF at smaller r ($<\sim$15 R_E), there is clear dawn-dusk asymmetry with the density (temperature) in the postmidnight sector being higher (lower) than that in the premidnight sector. However, as southward IMF proceeds the density asymmetry becomes weaker, because of significant decrease in the density in the postmidnight sector, while the temperature asymmetry remains. Across the tail at fixed X, relatively higher density and lower temperature near the flanks than near midnight are always seen regardless of the IMF conditions, and the dawn flank appears denser than the dusk flank. The dawn flank high-density region also appears less confined to large values of $|Y|$ than does the dusk flank region, and it extends to lower $|Y|$ with decreasing r as northward IMF proceeds and connects with the postmidnight high-density region. In general the above distributions and their differences between northward and southward IMF are consistent with the results of equatorial mapping of DMSP observations [*Wing and Newell*, 2002].

[11] The asymmetries seen in the density and temperature distributions can be explained by the different transport for low- and high-energy ions and the difference in the source distributions along the dawn and dusk flanks as will be discussed in 4.2. The significant change of the flank density with the IMF B_z direction suggests dependence of the particle source along the flanks on the IMF B_z as will be discussed in 4.3.

[12] The density and temperature distributions indicate that the pressure in the premidnight sector is mainly contributed by hotter and tenuous plasma while that in the post midnight sector are mainly by colder but denser plasma. The pressure has relatively weaker dawn-dusk asymmetry than do the density and temperature and depends more strongly on r, with higher pressure seen at smaller r. Slightly higher pressure in the premidnight sector than in the postmidnight sector can be seen at large r during northward IMF, but this asymmetry can be also seen at smaller r as southward IMF proceeds because of significant decrease of number density in the postmidnight near-Earth plasma sheet. The pressure in the region $|Y| < 2.5$ R_E and between $r = 8$ and 12 R_E that is seen to be distinctly higher than at other local times when southward IMF lasts longer than 1 hour is likely due to the contribution from energization associated with the substorm dipolarizations.

[13] Figure 3 shows the ratio of the standard deviation to the average and shows that the density has larger fluctua-

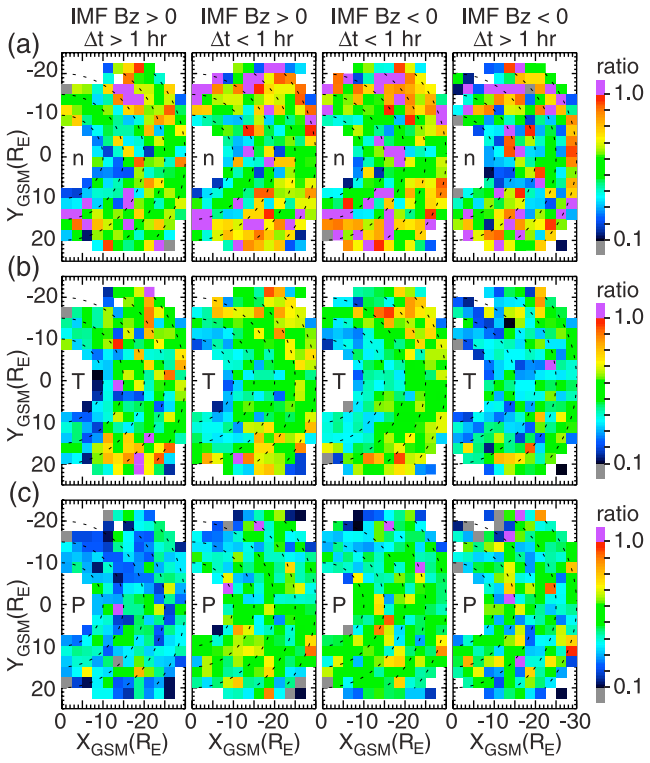

Figure 3. Ratio of the standard deviation to the average of (a) number density, (b) temperature, and (c) plasma pressure during the four IMF B_z conditions.

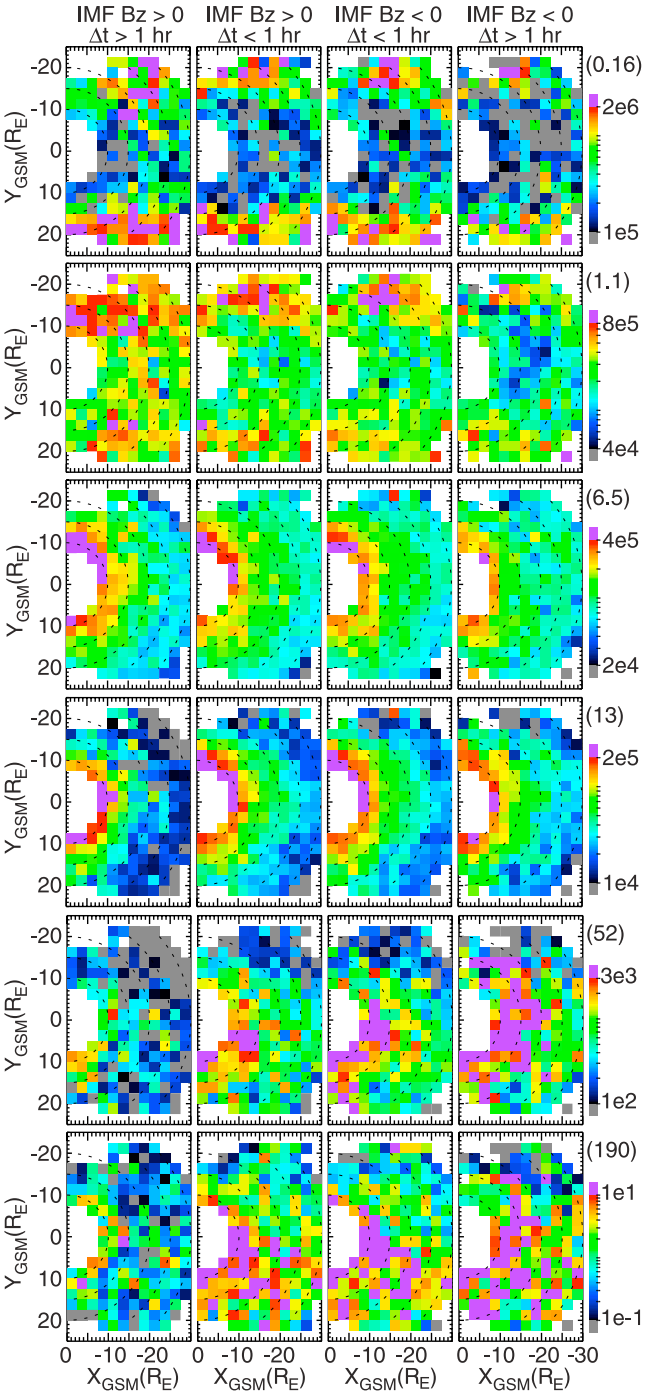

Figure 4. Equatorial distributions of differential flux ($(cm^2\ s\ sr\ keV)^{-1}$) for different energy ions (energy in keV, as indicated by the value above each color bar) during the four different IMF B_z conditions.

tions (their magnitude relative to the average values, the same for the fluctuations of other parameters discussed in this paper) than do the temperature and pressure. The density and temperature fluctuations are larger near the two flanks, while the pressure fluctuation is larger in the premidnight sector. For density and pressure, the fluctuation is smallest during northward IMF longer than 1 hour and largest during southward IMF longer than 1 hour, but the temperature fluctuation has the opposite dependence on the IMF conditions. The standard deviations also indicate that the spatial features discussed above are real since the fluctuations are smaller than the spatial variations in the features.

3.2. Fluxes

[14] To identify the different contributions from the ions of different energies to the observed distributions of density, temperature, and pressure shown above, we investigate the distributions of the differential flux of each of the 42 energy channels from 0.021 to 3005 keV q^{-1} (the energy range for each channel is given by *Mukai et al.* [1994] and *Williams et al.* [1994]). The equatorial distributions of the ion fluxes at 6 different energy channels representing low (0.16 and 1.1 keV), near thermal (6.5 and 13 keV), and high energy (52 and 190 keV) are plotted in Figure 4 to show the dependence of the overall flux value on the IMF B_z condition and the very different dawn-dusk asymmetries seen at various energies. It can be seen that the overall flux for the low-energy (high-energy) ions is higher (lower) during northward IMF than southward IMF, while the overall flux for the thermal energy ions does not change as significantly as do the low- and high-energy particles. For the high-energy particles, the flux difference between northward and southward IMF is seen to be larger as energy goes higher. For the thermal energy ions, the flux at smaller (larger) r is seen to be slightly lower (higher) during southward IMF.

[15] For the low-energy ions, the flux near the flanks is seen to be always relatively higher than that around midnight regardless of the IMF conditions and the flux values increase (decrease) as northward (southward) IMF proceeds. This contrast between flank and midnight is seen to weaken with increasing energy, more significantly at the dusk flank than at the dawn flank, as a result of decreasing flux near the flanks and increasing flux around midnight. The contrast, however, is not seen at energies higher than 3.2 keV. Thus the ions with energies lower than 3 keV are the major contributor to the high-density low-temperature regions near the flanks shown in Figure 2. When the northward IMF lasts longer than 1 hour, the high-flux region near the dawn flank is seen to extend to the postmidnight sector at smaller r and can reach regions closer to midnight at slightly higher energy (see 1.1 keV). However, the high-flux region near the dusk flank does not extend toward midnight with increasing energy as seen on the dawn flank. The dawn-dusk asymmetry becomes weaker when southward IMF proceeds because of significant flux decrease in the post-midnight sector and along the dawn flank, resulting in the weakening of the density asymmetry described in 3.1. This dawn-dusk flux asymmetry can be explained by ions' westward magnetic drift, as will be discussed in 4.2.

[16] For the ions above ~6 keV, the flux in general increases with decreasing r under all IMF conditions, but different dawn-dusk asymmetry is seen at different r and energy. In the region $r > 15\ R_E$, the cross-tail profile at fixed X shows that the flux around midnight is higher than that near the flanks, which is opposite to the cross-tail profiles of the low-energy ions, and the flux near the dusk flank is clearly higher than that near the dawn flank. As energy goes higher, the dawn-dusk asymmetry with higher flux in the premidnight sector intensifies. These asymmetries are stronger during southward IMF than during northward IMF. In

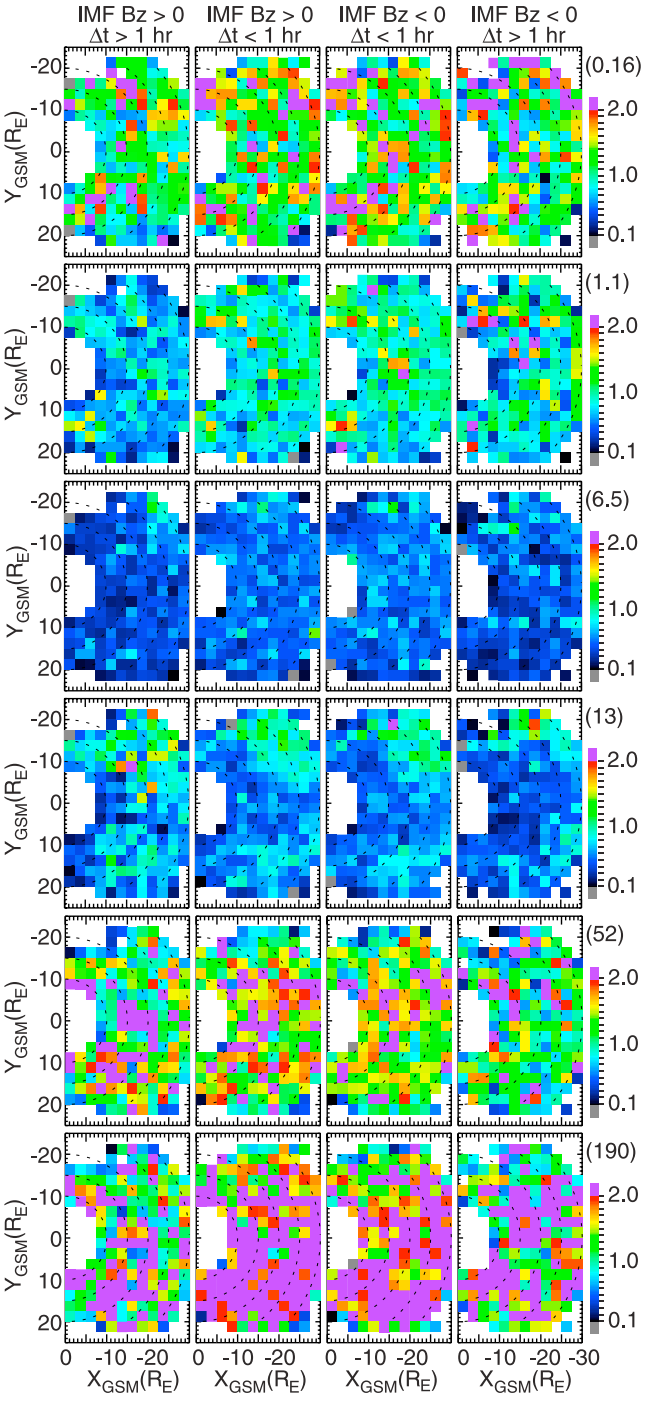

Figure 5. Ratio of the standard deviation to the average of differential flux for different energy ions (energy in keV, as indicated by the value above each color bar) during the four IMF B_z conditions.

the region $r < 15\ R_E$, the flux at thermal energies does not have strong dawn-dusk asymmetry as seen at low energy, regardless of the IMF conditions. However, the flux at high energies is seen to be higher in the premidnight sector during all the IMF conditions, which is a result of, as will be discussed in 4.2, the transport being dominated by westward magnetic drift and much fewer high-energy particles coming from the dawn flank than from the tail.

[17] Figure 5 shows the ratio of the standard deviation to the average of differential flux. The fluctuation is very small near the thermal energy (6.5 keV) but it becomes larger as energy increases or decreases and can become comparable to the average at very low (0.16 keV) or very high energy (190 keV). The overall fluctuations are seen to be smallest during northward IMF longer than 1 hour and largest during southward IMF longer than 1 hour at all energies except 13 keV. The fluctuations are generally smaller than the spatial variations discussed above, which indicates the above spatial features and dawn-dusk asymmetries are reliable.

3.3. Magnetic Fields

[18] Figure 6 shows magnetic field $|B_x|$, $|B_y|$, and B_z for different IMF B_z conditions. We deliberately plot the $|B_y|$ in $Y < 0$ in the positive value scale and that in $Y > 0$ in the negative value scale. Assuming field line symmetry with respect to the current sheet and the midnight meridian, the profiles shown in Figure 6 represent the plasma sheet magnetic configurations in the region above the current sheet. Note that locally B_x and B_y can have positive or negative values due to effects such as Geotail's position above or blow the current sheet, field-aligned currents, and

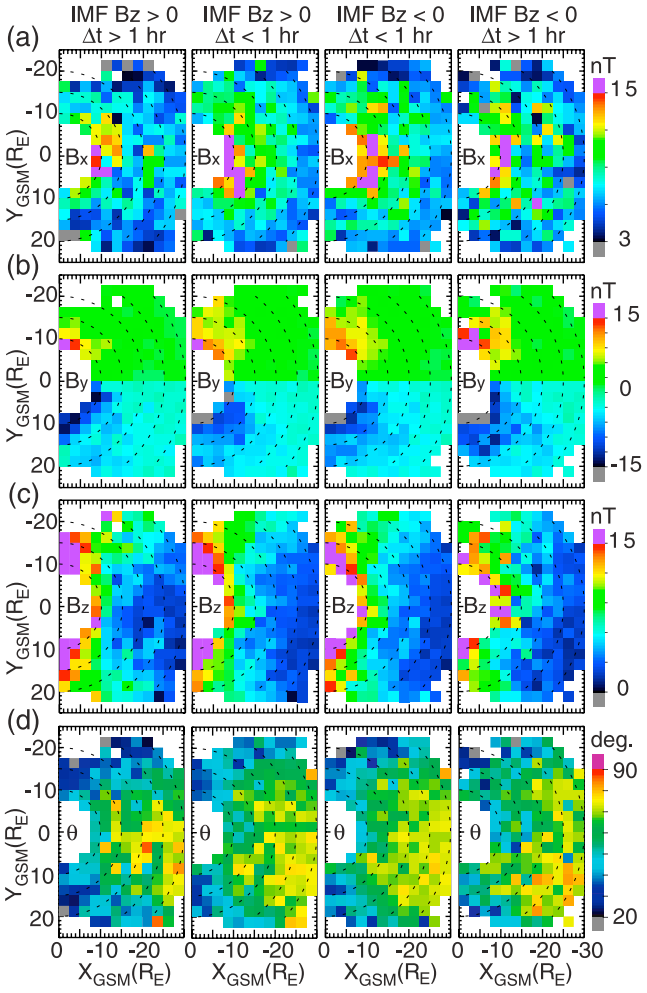

Figure 6. Equatorial distributions of (a) $|B_x|$, (b) $\pm|B_y|$, (c) B_z, and (d) θ ($\theta = \cos^{-1}(B_z/B)$) during the four IMF B_z conditions.

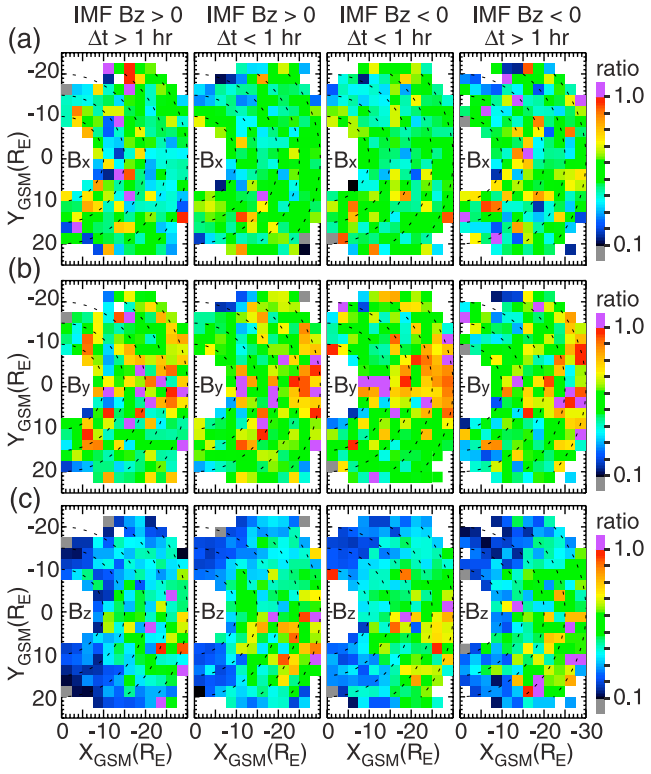

Figure 7. Ratio of the standard deviation to the average of (a) $|B_x|$, (b) $|B_y|$, and (c) B_z during the four IMF B_z conditions.

IMF penetration, so straight averages of B_x and B_y cannot well represent the large-scale magnetic field configuration.

[19] For northward IMF, the overall $|B_x|$ and $|B_y|$ for $\Delta t >$ 1 hour are smaller than those for $\Delta t < 1$ hour. However, the overall B_z for $\Delta t > 1$ hour is seen to be larger than that for $\Delta t < 1$ hour. Comparing the fields between the northward and southward IMF for $\Delta t < 1$ hour shows clearly that overall $|B_x|$ and $|B_y|$ are larger during southward IMF. The B_z during southward IMF is seen to be slightly larger at $r > 15\ R_E$ but smaller at $r < 15\ R_E$ than those seen during northward IMF, and the difference can be seen more clearly outside $|Y| = \sim 8\ R_E$. For southward IMF, the overall $|B_y|$ for $\Delta t > 1$ hour is larger than that for $\Delta t < 1$ hour. In the region $|Y| > 8\ R_E$, the B_z for $\Delta t > 1$ hour is smaller compared to that for $\Delta t < 1$ hour but no clear difference is seen in $|B_x|$. However, in the region $|Y| < 8\ R_E$, the $|B_x|$ for $\Delta t > 1$ hour is found to be smaller and B_z to be larger than those seen for $\Delta t < 1$ hour.

[20] That the overall $|B_x|$ and $|B_y|$ are stronger during southward IMF than northward IMF while the overall B_z does not change as significantly as do $|B_x|$ and $|B_y|$ is a result of field lines being more stretched during southward IMF. The stretching can be clearly seen in the changes of θ ($\theta = \cos^{-1}(B_z/B)$, θ is larger as field lines become more stretched) shown in Figure 6d. That the B_z during southward IMF is slightly larger at larger radial distance but smaller at smaller radial distance than those seen during northward IMF is consistent with the results from self-consistent simulations of plasma and magnetic field under different convection strength [e.g., *Wang et al.*, 2004]. The $|B_x|$ and B_z changes seen in the region $|Y| < 8\ R_E$ and $X > -15\ R_E$ as the southward IMF goes from $\Delta t < 1$ to $\Delta t > 1$ hour is likely due to substorm dipolarizations occurring during the longer southward IMF periods. The B_z is always seen to be slightly lower in the premidnight sector than the postmidnight sector regardless of the IMF conditions, and the asymmetry can be seen at smaller r during southward IMF than during northward IMF. This B_z asymmetry and its change with the IMF B_z conditions are expected from the force balance between the magnetic field and plasma pressure, with the plasma pressure being generally higher in the premidnight sector and the pressure asymmetry at smaller r being stronger during southward IMF than during northward IMF as shown in Figure 2. This dawn-dusk asymmetry is also clearly seen in the θ distributions.

[21] Figure 7 shows the ratio of the standard deviation to the average. The fluctuation in B_y is stronger than that in B_x and B_z. The B_y fluctuation is larger near midnight and at larger r, while that in B_z is larger in the premidnight sector and at larger r. The B_x fluctuation does not have strong dependence on location. The fluctuations in all three components do not change significantly with the IMF B_z condition. The fluctuations are smaller than the spatial variations we discussed, which indicates the reliability of the above spatial features in the magnetic fields.

3.4. Perpendicular Flow

[22] The top plots of Figure 8 show the perpendicular velocity for the different IMF B_z conditions. Note that only $|V_\perp| \leq 200$ km s^{-1} has been included in this study. For northward IMF longer than 1 hour, the overall flow speed is less than 50 km s^{-1}. Most of the flow in the $Y < 0$ region is mainly directed earthward and dawnward, while almost all the flow in the $Y > 0$ region is earthward and duskward. The flow is more earthward at larger $|Y|$. However, in the region $|Y| < \sim 10\ R_E$ there is a dawn-dusk asymmetry with larger flow speed at $Y > 0$ and smaller and less dawnward flow at $Y < 0$. The asymmetry becomes more significant with decreasing radial distance. The flow pattern indicates that the plasma from the tail near the midnight meridian diverts around the Earth to the dayside mainly through the dusk side.

[23] As the IMF condition changes form being shorter northward to shorter southward and then to longer southward, it can be seen the overall flow pattern described above does not change significantly. However, the flow speed everywhere increases gradually, with the overall speed for southward IMF $\Delta t > 1$ hour being about three times the speed for northward IMF $\Delta t > 1$ hour. These are consistent with the flow changes with increasing AE observed by ISEE [*Zhu*, 1993].

4. Discussion

4.1. Distribution of Electric Potential in the Plasma Sheet

[24] In the slow flow approximation, which is valid within the plasma sheet except during for dynamic periods such as the expansion phase of substorms, plasma drift results from electric drift $\mathbf{V}_E = (\mathbf{E} \times \mathbf{B})/B^2$ and diamagnetic drift $\mathbf{V}_{dia}$, where $\mathbf{E}$ is electric field and $\mathbf{B}$ is magnetic field. $\mathbf{V}_{dia} = (\mathbf{B} \times \nabla p)/(neB^2)$ for protons under the condition of

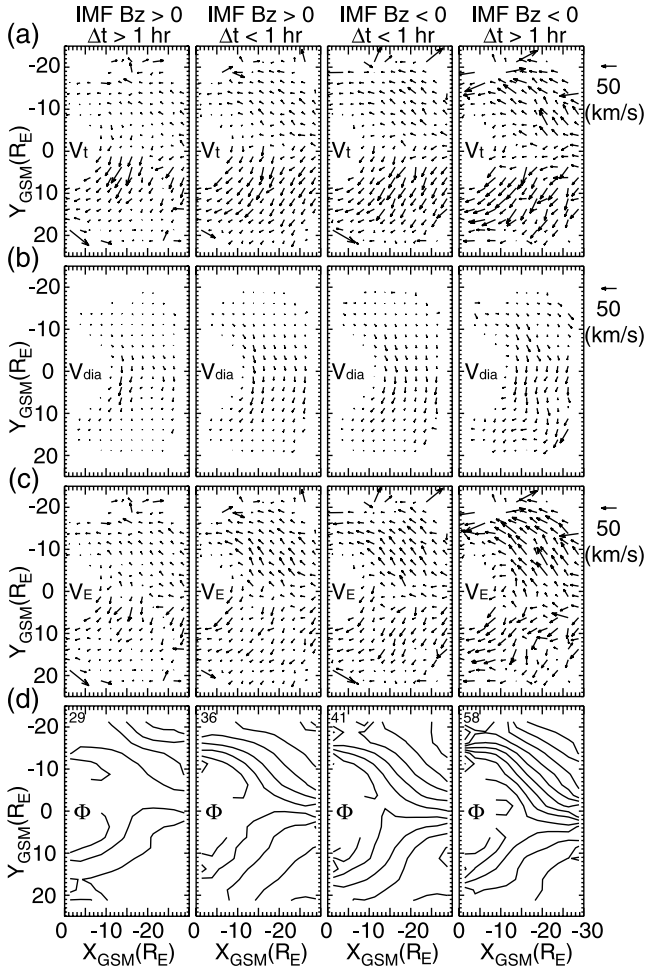

Figure 8. Equatorial distributions of (a) perpendicular flow, (b) diamagnetic drift, (c) electric drift, and (d) electric potential contours (5 kV intervals). The arrow at the top right corner represents a unit vector of 50 km s^{-1}. The values of the cross-tail potentials are indicated at the top left corner of each electric potential plot.

isotropic pressure, which is a good approximation for the plasma sheet plasma [e.g., *Stiles et al.*, 1978; *Nakamura et al.*, 1991], where p is plasma pressure and n is number density. The middle plots of Figure 8 show $\mathbf{V}_{dia}$ in the x-y directions at the center of the current sheet ($\mathbf{B} = B_z\hat{\mathbf{z}}$) using the n and p distributions shown in Figure 2 assuming all ions are protons, and the B_z distributions shown in Figure 6. The n, p, and B_z have been smoothed before computing $\mathbf{V}_{dia}$. $\mathbf{V}_{dia}$ is mainly directed westward because ∇p is mainly in the radial direction. The speed of $\mathbf{V}_{dia}$ is larger near midnight and at smaller r, and in these regions its magnitude is comparable to the total drift. The flow pattern for $\mathbf{V}_{dia}$ is similar for different IMF Bz conditions but its overall speed during southward IMF is stronger than that during northward IMF. It is evident that the dawn-dusk asymmetry seen at $|Y| < 10\ R_E$ in the total drift is mainly due to diamagnetic drift.

[25] The third rows of Figure 8 show the electric drift $\mathbf{V}_E$ computed from subtracting the total drift with the diamagnetic drift, and the bottom plots of Figure 8 show contours of electric potential integrated over electric field $\mathbf{E} = -\mathbf{V}_E \times \mathbf{B}$ at the center of the current sheet. (Note: there is electric field data measured by Geotail but it has an offset too large for the data to be suitable for our study). The electric drift shows that flow in the $Y < 0$ region is mainly directed earthward and dawnward, while the flow in the $Y > 0$ region is earthward and duskward. The electric drift pattern appears more dawn-dusk symmetric than does the total drift. The electric drift speed becomes larger, indicating stronger convection, as the IMF conditions change from longer to shorter northward, to shorter southward, then to longer southward. The potential difference between $Y = \pm 19\ R_E$ at $X = -26\ R_E$ is shown in the top left corner of each plot. The potential difference across the tail is stronger during southward than during northward IMF, as expected from the dependence of the cross–polar cap potential drop on the direction of the IMF B_z [e.g., *Weimer*, 1995], a clear indication of the control of magnetosphere convection by the IMF B_z. The contours of the electric potential at smaller X are less dense near midnight than near the flanks, indicating smaller electric field near midnight, a feature that is expected from the effect of shielding electric field near the inner edge of the plasma sheet. As the cross-tail potential increases, the region affected by the shielding is seen to retreat to smaller r, allowing the plasma from the tail to penetrate further earthward.

4.2. Electric and Magnetic Drift Transport

[26] In this section we investigate the different adiabatic drift transport and energization of different energy particles from the flanks and tail and determine if the resulting plasma distribution can account for the observed flux distributions. With the magnetic field B shown in Figure 6 and electric potential Φ shown in Figure 8, we evaluate the magnetic drift ($\mu\mathbf{B} \times \nabla B/eB^2$) and electric drift ($\mathbf{B} \times \nabla\Phi/B^2$) paths of protons of different first adiabatic invariants μ assuming all ions are protons and have 90 degree pitch angle, where B is the observed field strength and e is unit charge. μ is defined as E_k/B, where E_k is the particle's kinetic energy. In this paper, the unit for μ is chosen to be keV $(10\ nT)^{-1}$. 10 nT is approximately the field strength at $X = -15$ and $Y = 0\ R_E$, so the μ value indicates the energy that a particle would have in the plasma sheet. The drift paths are equivalent to the contours of constant $\mu B + e\Phi$. (Note: Magnetic drift also depends on the particle's pitch angle. For isotropic plasma particles, they conserve $E_k V^{2/3}$ along their bounce-averaged electric and magnetic drift paths [*Wolf*, 1983], where V is the flux tube volume per unit magnetic flux. Since a magnetic field model is needed to calculate V and we intend to conduct this investigation solely on the basis of observational data, we didn't investigate in this study the transport of particles that conserve $E_k V^{2/3}$.)

[27] Figure 9 shows the contours of $\mu B + e\Phi$ for 6 selected μ representing low (μ = 0.16 and 1.1 keV $(10\ nT)^{-1}$), near thermal (μ = 6.5 and 13 keV $(10\ nT)^{-1}$), and high energy (μ = 52 and 190 keV $(10\ nT)^{-1}$) particles for northward IMF longer than 1 hour (first column) and for southward IMF less than 1 hour (third column). To examine if these $\mu B + e\Phi$ paths represent the major transport, which would give constant phase space density for particles of a given μ along the constant $\mu B + e\Phi$ contours, we plot in the second and fourth columns of Figure 9 the distributions of

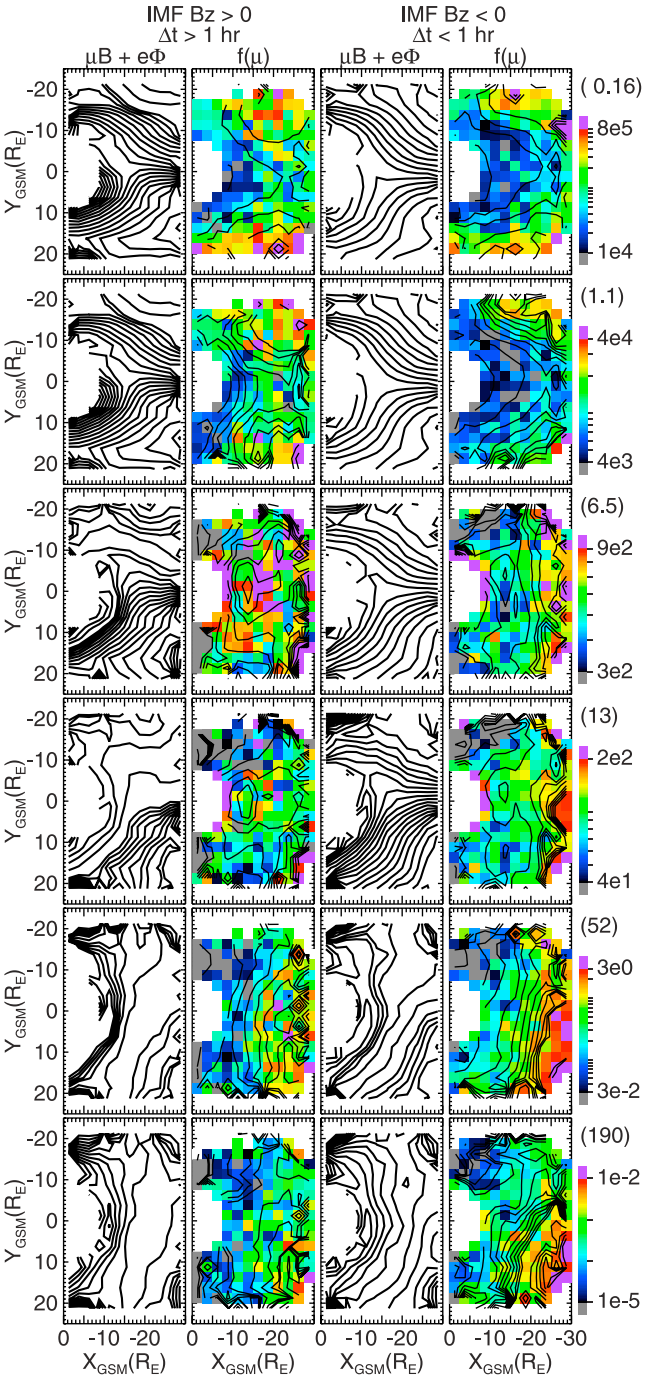

Figure 9. Comparison between drift paths ($\mu B + e\Phi$) and the distributions of phase space density $f(\mu)$ (normalized by 1.5×10^{-15} m^{-3} (m s^{-1})$^{-3}$) for different μ (μ value in keV (10 nT)$^{-1}$, as indicated by the number above each color bar) during longer than 1 hour northward IMF and shorter than 1 hour southward IMF.

the phase space density f and contours of constant f for the same μ, computed from the 42 energy channels of observed differential fluxes j ($f = j \cdot 2E_k/m^2$, where m is the proton mass).

[28] For very low-energy particles (μ = 0.16 keV (10 nT)$^{-1}$), the total drift paths are very similar to the Φ contours shown in Figure 8 because the drift is dominated by electric drift. Because of the shielding effect at the inner edge of plasma sheet, as the low-energy particles from the tail move further earthward they are pushed toward larger $|Y|$ so they have much less access to $r < 15\ R_E$. This is in very good agreement with the observed f distributions, which show relatively low f in the region of $r < 15\ R_E$, and with the similarity between the contours of $\mu B + e\Phi$ and of f for both northward and southward IMF conditions. The agreement confirms the general features of the electric potential pattern we inferred from the observations. These low-energy particles divert toward the flanks as they drift earthward, resulting in the plasma sheet being colder and denser near the flanks than around midnight as shown by Figure 2.

[29] For particles of slightly higher energy but still below the thermal (μ = 1.1 keV (10 nT)$^{-1}$), the drift paths are similar to the ones for μ = 0.16 keV (10 nT)$^{-1}$. However, with slightly higher westward magnetic drift, the particles can penetrate deeper into the near-Earth plasma sheet in the postmidnight sector than in the premidnight sector. This accounts for the dawn-dusk asymmetry in the near-Earth plasma sheet seen in the density shown in Figure 2 and in the flux for ions <3 keV shown in Figure 4, and that the high-density region near the dawn flank extends to smaller $|Y|$ than does the high-density region near the dusk flank shown in Figure 2 when the IMF is northward. However, this dawn-dusk asymmetry is much weaker during southward IMF when electric drift is too strong for magnetic drift to alter the paths of these low-energy ions.

[30] For the particles near the thermal energy (μ = 6.5 and 13 keV (10 nT)$^{-1}$), the drift paths are very different from the drift paths seen for the low-energy particles, especially in the near-Earth plasma sheet, because of stronger magnetic drift. A significant difference can be seen in that particles of these energies from the tail have access to the midnight region at smaller r (<15 R_E), a region that cannot be readily accessed by the low-energy particles. These particles first drift earthward in the postmidnight sector to smaller r and then are diverted toward the dusk sector by the increasing westward magnetic drift. This is seen in the f distribution around midnight as the f at smaller r having similar magnitude to the f in the tail. Because of the path diversion by magnetic drift, the region in the $Y < -10\ R_E$ in the near-Earth plasma sheet cannot be readily accessed by particles from the tail but can be reached by those from the dawn flank. This, combined with f along the dawn flank being much lower than f in the tail, results in the f in the $Y < -10\ R_E$ region near dawn being relatively lower than f near dusk and in the tail. Therefore the drift paths can explain the important dawn-dusk asymmetry seen in the distribution of f of the near thermal particles.

[31] For the high-energy particles (μ = 52 and 190 keV (10 nT)$^{-1}$), the drift is dominated by the westward magnetic drift. This makes the postmidnight sector accessible mostly by particles from the dawn flank and the premidnight sector accessible mostly by particles from the tail. The paths are confirmed by the general agreement with the constant f contours. That the number of the high-energy particles from the dawn flank is much smaller than that from the tail results in the dawn-dusk flux asymmetry for the high-energy ions seen in Figure 4. This, together with the asymmetry seen in the

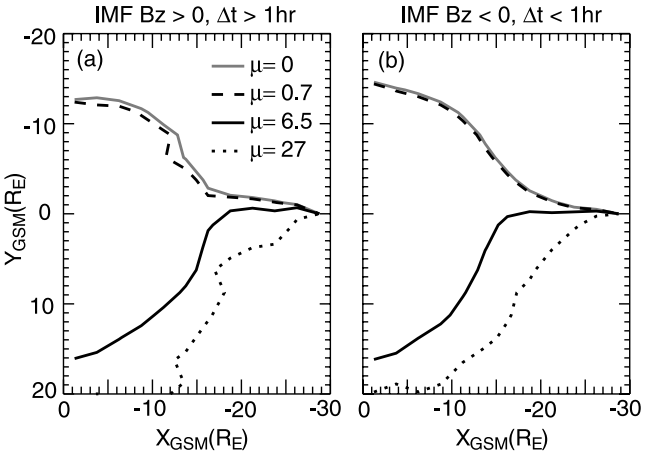

Figure 10. Comparison of the trajectories of ions of different energies (μ value in keV (10 nT)$^{-1}$) coming from a same location at X = −28.5 R_E and $Y = 0$ R_E following the drift paths ($\mu B + e\Phi$) during (a) northward IMF longer than 1 hour and (b) southward IMF shorter than 1 hour.

near-thermal particles, accounts for the higher temperature in the premidnight sector seen in Figure 2.

[32] The above phase density distributions as a function of ion energy invariant are in qualitative agreement with the results of *Garner et al.* [2003] that is based on earlier statistical studies of plasma sheet parameters. Figure 10 compares the trajectories of ions of different energies coming from the same location at $X = -28.5$ R_E and $Y = 0$ R_E following the drift paths $\mu B + e\Phi$ obtained from our analysis, which clearly shows how large the effect of magnetic drift can become, as particles' energy become higher, in diverting particles away from their electric drift paths. It is important to point out that, as shown in Figure 10, for typical thermal energy ions (μ = 6.5 keV (10 nT)$^{-1}$) in the plasma sheet, their magnetic drift has become as strong as electric drift in determining their transport and energizaton.

[33] The consistency between the constant f contours and drift paths for the thermal energy ions (μ = 6.5 and 13 keV (10 nT)$^{-1}$) is not as good as those for the low- and high-energy ions, especially in the near Earth region around midnight ($X > -20$ R_E, $|Y| < 10$ R_E). A possible cause for this is variations of convection strength. The magnitude of electric drift changes with convection strength, but its direction may remain similar. Therefore changing convection strength can have a stronger effect on the direction of total drift for thermal energy ions around midnight because their drift there, as shown in Figure 10, results from the competition between electric and magnetic drifts having similar magnitudes. This should have a smaller effect on the direction of total drift for the low-energy ions, which is dominated by electric drift, and for the high-energy ions, which is dominated by magnetic drift. Stronger change in the drift transport direction for the thermal energy ions can lead to a distribution having constant f contours that are less parallel to the average drift direction. This explanation will be further investigated in the future with data sorting according to similar convection strength.

[34] It is interesting that, for the thermal energy ions during IMF $B_z < 0$, f in the tail ($X < -25$ R_E) is larger than that in the near Earth ($X > -15$ R_E) along the same drift path. That the f in the tail is not totally transport earthward has been pointed out in previous studies [e.g., *Garner et al.*, 2003] and has been related to the topic of the pressure balance inconsistency [*Erickson and Wolf*, 1980]. The high f in the tail and the strong drop along drift paths are likely to be associated with processes other than the slow drift transport, such as bursty flow, formation of bubbles and blobs, substorms, and reconnection [e.g., *Kaufmann et al.*, 2004a]. That these processes are less frequently observed during northward IMF may explain why the strong f drop is not seen in Figure 9 for IMF $B_z > 0$. Our results can be used in the future to compare with simulations that include these processes.

4.3. Cold Ion Source Along the Flanks

[35] We found from the distributions of f for μ = 0.16 keV (10 nT)$^{-1}$ shown in Figure 9 that f near the flanks appears to have larger values than f in the tail along a given drift path (constant $\mu B + e\Phi$) when the IMF is northward, but the difference is small when the IMF is southward. We compare in Figure 11 the f along the dawn and dusk flanks at $|Y| = 20$–22.5 R_E and $X > -25$ R_E with the f in the tail at $X = -27.5 - (-30)$ R_E and $|Y| < 20$ R_E for μ < 1 keV (10 nT)$^{-1}$. It can be clearly seen that, during northward IMF, for μ ∼ 1 keV (10 nT)$^{-1}$ there is almost no difference between f along the flanks and that in the tail. However, as particle energy goes lower, f along the flanks becomes larger than f

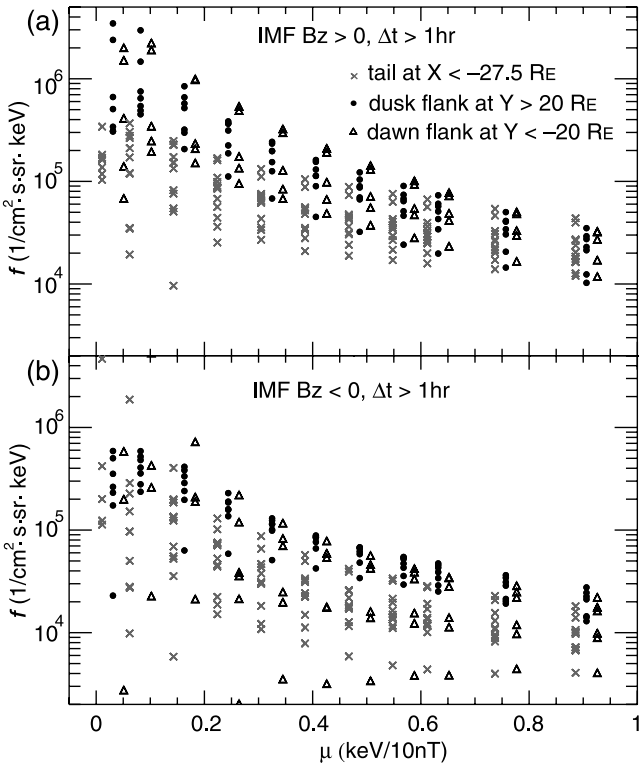

Figure 11. Comparison of the phase space density at the tail ($X = -27.5 - (-30)$ R_E, $|Y| < 20$ R_E) with that along the dawn ($0 > X > -25$ R_E, $Y = -20 - (-22.5)$ R_E) and dusk ($0 > X > -25$ R_E, $Y = 20$–22.5 R_E) flanks for μ < 1 keV (10 nT)$^{-1}$ during (a) northward IMF longer than 1 hour and (b) southward IMF longer than 1 hour.

in the tail and is about one magnitude larger for $\mu \sim 0.1$ keV $(10\ \mathrm{nT})^{-1}$. During southward IMF, the difference is also seen to become larger with lower energy but the difference is much smaller than that during northward IMF.

[36] That the f for very low energy ions along the flanks is larger than that can be transported from the tail, and the difference is larger for lower energy, indicates existence of a cold particle source along the flanks at $X > -30\ R_E$. The cold flank particle source can be provided by direct entry of the magnetosheath particles, which have a typical temperature <0.1 keV, into the plasma sheet through the flanks. The difference between northward and southward IMF also suggests that the flank source is weaker during southward IMF, indicating the physical processes responsible for the source are more effective during northward IMF.

5. Summary

[37] We have investigated statistically the equatorial distributions of the ion moments, fluxes, and magnetic fields measured by Geotail in the nightside plasma sheet when the IMF B_z has been continuously northward or southward for less than or more than 1 hour to evaluate the ion population and magnetic field as a function of location and the IMF B_z conditions, and to determine if the electric and magnetic drift transport and the associated adiabatic energization of ions from the tail and flanks can account for these distributions.

[38] In the near-Earth plasma sheet during northward IMF, there is strong dawn-dusk asymmetry in the density and temperature distributions with higher density and lower temperature in the postmidnight sector, which results in weak dawn-dusk pressure asymmetry. However, as southward IMF proceeds, the density asymmetry weakens while the temperature maintains, resulting in higher pressure in the premidnight sector. Across the tail at fixed X, the density (temperature) is found to be relatively higher (lower) near the flanks than around midnight regardless of the IMF B_z conditions.

[39] The distributions of flux are significantly different for different energy ions. In the near-Earth plasma sheet, flux is higher in the postmidnight sector for low-energy ions but higher in the premidnight sector for high-energy ions. Across the tail at fixed X, the ions $<\sim$3 keV have higher flux along the flanks than around midnight, but as energy goes higher, the region of high flux is seen more dominantly in the premidnight sector.

[40] The magnetic fields indicate that the field lines are more stretched during southward IMF than northward IMF, and the field lines become further (less) stretched as southward (northward) IMF proceeds. There is weak dawn-dusk asymmetry with lower B_z in the premidnight sector than the postmidnight sector, resulting from force balance with the plasma pressure.

[41] The perpendicular flow at $|Y| < \sim 10\ R_E$ is seen to be stronger in the premidnight sector, and this dawn-dusk asymmetry becomes stronger with decreasing radial distance, indicating the ions from the tail divert around the Earth mainly through the dusk side. The asymmetry results from westward diamagnetic drift. The flow pattern does not change significantly with the IMF B_z conditions but the overall flow speed for southward IMF $\Delta t > 1$ hour is about three times the speed for northward IMF $\Delta t > 1$ hour.

[42] We inferred the plasma sheet electric fields and electric potentials from the electric drift, which we obtained by subtracting the diamagnetic drift computed using the observed density, pressure, and magnetic field from the measured total flow. The equatorial electric potential pattern shows the effect of the shielding electric field in the inner plasma sheet. The cross-tail potential drop for southward IMF $\Delta t > 1$ hour is about twice that for northward IMF $\Delta t > 1$ hour.

[43] With the observed magnetic field and the inferred electric field, we determined the electric and magnetic drift paths for ions of different first adiabatic invariants μ and compare the paths with the distributions of the phase space density of these μ. The transport of low-energy ions is dominated by electric drift, while magnetic drift dominates the transport of high-energy ions. For near thermal energy ions, the magnetic drift is as important as electric drift. We examined if the distribution of the observed phase space density throughout the nightside plasma sheet can be accounted for by transporting ions from the tail at $X \sim -30\ R_E$ and the flanks at $|Y| > 20\ R_E$ and conserving their phase space density along their electric and magnetic drift paths. We found very good agreement between the constant phase space density contours and drift paths at the low and high energy. For the thermal energy, we found that the drift paths can explain the dawn-dusk asymmetry of the phase space distributions. These agreements indicate that the electric and magnetic drift play a major role in the plasma transport and energization in the plasma sheet, and are responsible for the observed dawn-dusk asymmetries in the plasma and magnetic field distributions. However, the agreement is not as good around midnight at thermal energy as at low and high energy, which could result from strong variations of the total drift direction in response to variations in convection strength. We also found that, for thermal energy ions during IMF $B_z < 0$, not all the particles in the tail are transported earthward along their drift paths, which could be a result of transport processes other than the slow adiabatic drift considered here.

[44] We found that the phase space density for <0.5 keV ions along the flanks is significantly larger than that can be transported from the tail during northward IMF, indicating contribution from a cold particle source along the flanks at $X > -30\ R_E$ that could be provided by direct entry of the magnetosheath particles into the plasma sheet through the flanks.

[45] **Acknowledgments.** The work by C.-P. Wang and L. R. Lyons has been supported by NSF grant ATM-0207298. The work by J. M. Weygand has been supported by NSF GEM ATM-0201798. The work by R. W. McEntire has been supported by NASA grant NNG04GC23G. We thank T. Mukai at ISAS and CDAWeb for the use of the Geotail LEP data and S. Kokubun at STELAB Nagoya University, Japan, and CDAWeb for the use of Geotail magnetic field data. We thank Jon Vandegriff of the Applied Physics Laboratory for providing the Geotail EPIC data. We also thank Dan Weimer for providing the Weimer variance analysis routine.

[46] Wolfgang Baumjohann thanks Richard L. Kaufmann and Lynn Kistler for their assistance in evaluating this paper.

References

Angelopoulos, V. (1996), The role of impulsive particle acceleration in magnetotail circulation, in *Proceedings of the Third International Conference on Substorms (ICS-3)*, *Eur. Space Agency Spec. Publ., ESA-SP 389*, 17–22.

Angelopoulos, V., et al. (1993), Characteristics of ion flow in the quiet state of the inner plasma sheet, *Geophys. Res. Lett.*, *20*, 1711–1714.

Erickson, G. M., and R. A. Wolf (1980), Is steady convection possible in the Earth's magnetotail?, *Geophys. Res. Lett.*, *7*, 897–900.

Fujimoto, M., T. Terasawa, and T. Mukai (1998), The low-latitude boundary layer in the tail-franks, in *New Perspectives on the Earth's Magnetotail*, *Geophys. Monogr. Ser.*, vol. 105, edited by A. Nishida, D. N. Baker, and S. W. H. Cowley, pp. 33–44, AGU, Washington D. C.

Garner, T. W., R. A. Wolf, R. W. Spiro, M. F. Thomsen, and H. Korth (2003), Pressure balance inconsistency exhibited in a statistical model of magnetospheric plasma, *J. Geophys. Res.*, *108*(A8), 1331, doi:10.1029/2003JA009877.

Guild, T., et al. (2004), Plasma sheet climatology: Geotail observations and LFM model comparisons, *J. Atmos. Sol. Terr. Phys.*, *66*(15–16), 1351–1360.

Kaufmann, R. L., W. R. Paterson, and L. A. Frank (2004a), Pressure, volume, density relationships in the plasma sheet, *J. Geophys. Res.*, *109*, A08204, doi:10.1029/2003JA010317.

Kaufmann, R. L., W. R. Paterson, and L. A. Frank (2004b), Magnetization of the plasma sheet, *J. Geophys. Res.*, *109*, A09212, doi:10.1029/2003JA010148.

Kokubun, S., T. Yamamoto, M. H. Acuna, K. Hayashi, K. Shiokawa, and H. Kawano (1994), The Geotail magnetic field experiment, *J. Geomagn. Geoelectr.*, *46*, 7–21.

Mukai, T., S. Machida, Y. Saito, M. Hirahara, T. Terasawa, N. Kaya, T. Obara, M. Ejiri, and A. Nishida (1994), The low-energy particle (LEP) experiment onboard the Geotail satellite, *J. Geomagn. Geoelectr.*, *46*, 669–692.

Nakamura, M., G. Paschmann, W. Baumjohann, and N. Sckopke (1991), Ions distributions and flows near the neutral sheet, *J. Geophys. Res.*, *96*, 5631–5649.

Paterson, W. R., L. A. Frank, S. Kokubun, and T. Yamamoto (1998), Geotail survey of ion flow in the plasma sheet: Observations between 10 and 50 R_E, *J. Geophys. Res.*, *193*, 11,811–11,825.

Spence, H. E., and M. G. Kivelson (1993), Contributions of the low-latitude boundary layer to the finite width magnetotail convection model, *J. Geophys. Res.*, *98*, 15,487–15,496.

Stiles, G. S., E. W. Hones Jr., S. J. Bame, and J. R. Asbridge (1978), Plasma sheet pressure anisotropies, *J. Geophys. Res.*, *83*, 3166–3172.

Terasawa, T., et al. (1997), Solar wind control of density and temperature in the near-Earth plasma sheet: Wind/Geotail collaboration, *Geophys. Res. Lett.*, *24*, 935–938.

Thomsen, M. F., J. E. Borovsky, R. M. Skoug, and C. W. Smith (2003), Delivery of cold, dense plasma sheet material into the near-Earth region, *J. Geophys. Res.*, *108*(A4), 1151, doi:10.1029/2002JA009544.

Tsyganenko, N. A., and T. Mukai (2003), Tail plasma sheet models derived from Geotail particle data, *J. Geophys. Res.*, *108*(A3), 1136, doi:10.1029/2002JA009707.

Wang, C.-P., L. R. Lyons, M. W. Chen, R. A. Wolf, and F. R. Toffoletto (2004), Modeling the transition of the inner plasma sheet from weak to enhanced convection, *J. Geophys. Res.*, *109*, A12202, doi:10.1029/2004JA010591.

Weimer, D. R. (1995), Models of high-latitude electric potentials derived with a least error fit of spherical harmonic coefficients, *J. Geophys. Res.*, *100*, 19,595–19,608.

Weimer, D. R., D. M. Ober, N. C. Maynard, M. R. Collier, D. J. McComas, N. F. Ness, C. W. Smith, and J. Watermann (2003), Predicting interplanetary magnetic field (IMF) propagation delay times using the minimum variance technique, *J. Geophys. Res.*, *108*(A1), 1026, doi:10.1029/2002JA009405. (Correction, *J. Geophys. Res.*, *109*, A12104, doi:10.1029/2004JA010691, 2004.)

Williams, D. J., R. W. McEntire, C. Schlemm II, A. T. T. Lui, G. Gloeckler, S. P. Christon, and F. Gliem (1994), GEOTAIL energetic particles and ion composition instrument, *J. Geomagn. Geoelectr.*, *46*, 39–57.

Wing, S., and P. T. Newell (1998), Central plasma sheet ion properties as inferred from ionospheric observations, *J. Geophys. Res.*, *103*, 6785–6800.

Wing, S., and P. T. Newell (2002), 2D plasma sheet ion density and temperature profiles for northward and southward IMF, *Geophys. Res. Lett.*, *29*(9), 1307, doi:10.1029/2001GL013950.

Wolf, R. A. (1983), The quasi-static (slow-flow) region of the magnetosphere, in *Solar Terrestrial Physics*, edited by R. L. Carovillano and J. M. Forbes, pp. 303–368, Springer, New York.

Zhu, X. (1993), Magnetospheric convection pattern and its implications, *J. Geophys. Res.*, *98*, 21,291–21,296.

L. R. Lyons and C.-P. Wang, Department of Atmospheric and Oceanic Sciences, University of California, MS-71, 405 Hilgard Avenue, Los Angeles, CA 90095-1565, USA. (cat@atmos.ucla.edu)

R. W. McEntire, Johns Hopkins University Applied Physics Laboratory, 11100 Johns Hopkins Road, Laurel, MD 20723-6099, USA.

T. Nagai, Department of Earth and Planetary Sciences, Tokyo Institute of Technology, Okayama 2-12-1 Meguro, Tokyo 152-8551, Japan.

J. M. Weygand, Institute of Geophysics and Planetary Physics, University of California, 3845 Slichter Hall, PO Box 951567, Los Angeles, CA 90095-1567, USA.